university of groningen

University Medical Center Groningen

University of Groningen

Magnetic order from molecular oxygen anions

Riyadi, Syarif

IMPORTANT NOTE: You are advised to consult the publisher's version (publisher's PDF) if you wish to cite from it. Please check the document version below.

Document Version
Publisher's PDF, also known as Version of record

Publication date:
2012

Link to publication in University of Groningen/UMCG research database

Citation for published version (APA):
Riyadi, S. (2012). *Magnetic order from molecular oxygen anions*. s.n.

Copyright
Other than for strictly personal use, it is not permitted to download or to forward/distribute the text or part of it without the consent of the author(s) and/or copyright holder(s), unless the work is under an open content license (like Creative Commons).

The publication may also be distributed here under the terms of Article 25fa of the Dutch Copyright Act, indicated by the “Taverne” license. More information can be found on the University of Groningen website: https://www.rug.nl/library/open-access/self-archiving-pure/taverne-amendment.

Take-down policy
If you believe that this document breaches copyright please contact us providing details, and we will remove access to the work immediately and investigate your claim.

Downloaded from the University of Groningen/UMCG research database (Pure): http://www.rug.nl/research/portal. For technical reasons the number of authors shown on this cover page is limited to 10 maximum.

Download date: 25-04-2025

Chapter 5

Isotropic S = 1/2 Antiferromagnetic Chain in p-Electron System

5.1 Introduction

Low-dimensional magnetic materials have been of particular interest in condensed matter physics. Low-dimensional magnetism mainly emerges in insulating materials, where the spins are localized at the atomic sites. Low-dimensional magnets often show peculiar physical properties, which triggers further investigation from both an experimental and theoretical perspective. For example, the quasi-2D antiferromagnetic material, La_2CuO_4, also behaves as a high-temperature superconductor [1]. Strong quantum fluctuations are believed to play a role in the magnetoelectric coupling exhibited by helimagnets with 1D chain crystal structures [2, 3]. Indeed, this has been shown experimentally by Seki et al. in the 1D spin-spiral system $CuCl_2$ [4]. Low-dimensional magnetism can also arise in a 3D crystal structure. Perhaps the best known of such systems is the 1D S = 1/2 antiferromagnetic chain in the 3D perovskite $KCuF_3$ [5–7]. In $KCuF_3$, the Jahn-Teller effect drives orbital ordering, thus creating magnetic exchange interactions only in one specific direction of the lattice. Here the magnetic properties are consistent with the theory of Kugel and Khomskii, which describes how orbital ordering drives the superexchange mechanism in systems with orbital degrees of freedom [8].

The hallmark of low-dimensional magnetism is the appearance of a broad maximum in the magnetic susceptibility versus temperature curve. It is rather difficult

A manuscript based on this chapter has been submitted for publication.

to distinguish between 1D and 2D magnets, since both show a broad maximum in susceptibility around the ordering temperature. Polynomial models have been developed to help experimentalists to identify the type of magnetic ordering in their compounds [9–11]. The most general model is probably the polynomial model of Keith et al. [12] which can distinguish both 1D and 2D low dimensional antiferromagnetic and ferromagnetic magnetic systems. Bonner and Fisher first described the linear chain system using the Heisenberg model [13]. The first compound shown to have one-dimensional linear chain magnetic ordering was probably $Cu(NH_3)_4SO_4.H_2O$, in which the qualitative model for the fitting of experimental magnetization data was formulated by Griffiths [13–17]. The 1D antiferromagnetic spin chain nature in $KCuF_3$ has also been well understood. The magnetism in both compounds originates from Cu, which is a d-electron metal. In this chapter I will explore the possibility of obtaining low-dimensional ordering driven by orbital ordering in a p-electron system.

At low temperatures, alkali metal superoxides (AO_2; A = K, Rb, Cs) show long-range magnetic ordering [18]. In the same way as many d-electron systems, the lattice, orbital, and spin degrees of freedom probably determine the magnetic properties. The orbital degeneracy in alkali metal superoxides is lifted by distortion of the crystal structure in the same way as the Jahn-Teller effect in transition metal compounds. In AO_2 this mainly involves the tilting or re-orientation of the superoxide dumbbells, thus altering the magnetic exchange interactions. The different dumbbell tilt systems result for example in long-range order below 7 K in KO_2 involving inter-plane antiferromagnetic superexchange and in-plane ferromagnetic direct exchange [19], and possible short-range magnetic order in NaO_2 [20].

In this chapter I will show, for the first time, the presence of low-dimensional magnetism in an inorganic p-electron system. To be more specific, a S = 1/2 1D antiferromagnetic spin chain has been established in cesium superoxide (CsO_2). CsO_2 adopts a rock-salt-type structure (e.g. NaCl) at room temperature in which superoxide dumbbells aligned parallel to the *c*-axis replace Cl^-. CsO_2 is reported to have long-range antiferromagnetic ordering below 9.6 K [21] on the basis of EPR and specific heat experiments (see Figure 5.1(a)) [18, 21]. Nevertheless, a broad minimum centered at ∼25 K was evident in the inverse susceptibility curve of CsO_2 and was not discussed in detail (see Figure 5.1(b)). In this chapter, I reinvestigate the magnetic properties of CsO_2 and show that one-dimensional antiferromagnetic ordering in CsO_2 sets in around 28 K. This represents the first example of a linear spin chain driven by orbital ordering in an inorganic p-electron magnetic system. I will examine the structural properties of this material as a function of temperature and show that the spin chain is induced by orbital ordering.

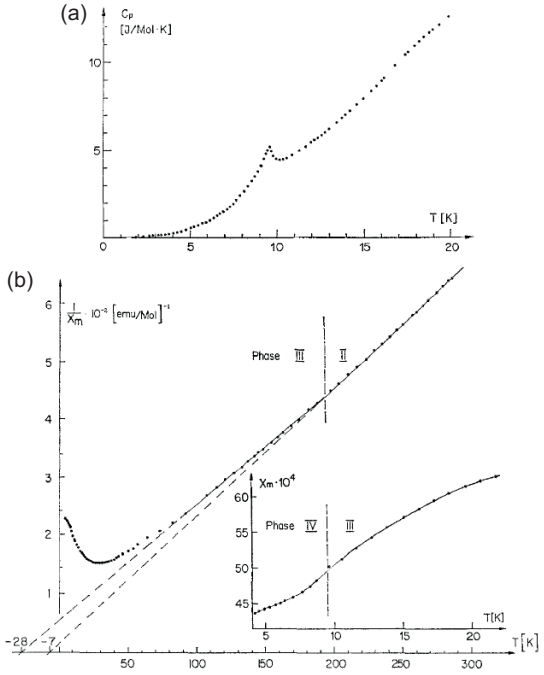

Figure 5.1. (a) Specific heat of CsO_2 below 20 K. (b) The inverse magnetic susceptibility as a function of temperature for CsO_2. Inset: the dashed line indicates the onset of 3D antiferromagnetic order below 9.6 K. These figures are taken from [21].

5.2 Experiment

Polycrystalline CsO_2 was prepared by careful oxidation of cesium metal dissolved in liquid ammonia. Cesium metal (Alfa-Aesar Chem., 95%, ∼1 g) was put in a 100 ml round bottom flask. Due to the high reactivity of this metal, it was handled in an atmosphere of dry nitrogen inside a glove box in which the water and oxygen concentration was always kept below 0.1 ppm. To exclude contamination from air moisture and CO_2, the synthesis of CsO_2 was carried out in a vacuum line.

Water-free liquid ammonia as a solvent was condensed into the round bottom flask at -65°C. A cryo-cooled ethanol solution was used as a cold bath. Dissolved cesium metal produced a dark blue solution, which indicates the presence of solvated electrons. Dry oxygen was then flowed through the reaction vessel, maintaining a pressure of 500-600 mmHg. The solution was continuously stirred during both the condensation of liquid ammonia and oxidation of the solution. The solution turned yellow after 2 hours of oxidation. The solution was then taken to room temperature to let the ammonia evaporate while continuing the oxygen flow. After the liquid ammonia had evaporated, the oxygen flow was continued for another 2 hours.

The yellow powder obtained was then subjected to various examination / characterization techniques. X-ray powder diffraction was performed using a Huber G670 diffractometer from room temperature down to 20 K. For magnetic measurements, the sample was flame sealed in an evacuated NMR tube, which was placed in a superconducting quantum interference device (Quantum Design SQUID MPMS-XL 7) magnetometer. Raman spectra were measured in a backscattering configuration using a liquid nitrogen-cooled charged coupled device (CCD), which was connected to a three-grating micro-Raman spectrometer (T64000 Jobin Yvon). Details of these techniques are given in Chapter 2.

5.3 Structure and Chemical Composition

The synthesis route described above yielded polycrystalline CsO_2. Like RbO_2 and KO_2, CsO_2 adopts the structure of CaC_2: space group $I/4mmm$. Figure 5.2 shows the fitted x-ray diffraction pattern of CsO_2 at room temperature, with lattice parameters of $a = b = 4.46164(6)$ $\AA$ and $c = 7.3310(1)$ $\AA$ (wRp = 0.0152). The refined structural parameters are tabulated in Table 5.1 and are in agreement with those reported for single crystal CsO_2 [21]. At room temperature the dioxygen anions are oriented along the c-axis of the cell (O-O distances ∼1.31 $\AA$). An impurity phase ($CsOH.H_2O$, space group $P6/mmm$, ∼20% by weight) was also present but does not contribute to the magnetic response of the sample.

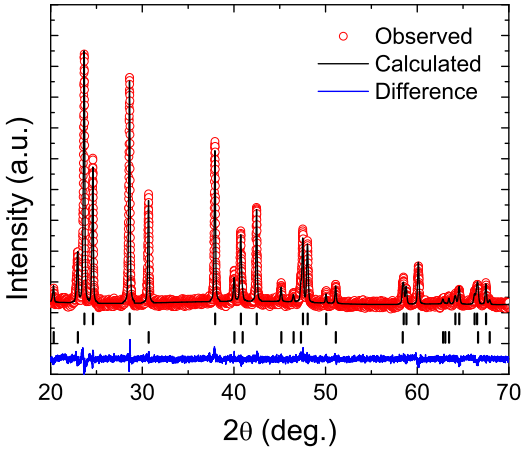

Figure 5.2. Observed (open circles), calculated (line) and difference (bottom line) x-ray powder diffraction profiles of CsO_2 at room temperature. The upper tick-marks indicate CsO_2 and the lower tick-marks indicate $CsOH.H_2O$.

Table 5.1. Room temperature refined structural parameters of CsO_2.

Atoms	x	y	z	U_{iso}
Cs($2a$)	0.5	0.5	0.5	0.04273(42)
O($4e$)	0	0	0.41036(14)	0.02541(21)

Raman spectra measured at room temperature (see Figure 5.3) showed a sharp, intense peak at ∼1134 cm^{-1}, which can be assigned to the stretching mode of the superoxide dumbbell [22]. This stretching mode is at lower frequency than in other alkali metal superoxides (NaO_2: 1164 cm^{-1}, KO_2: 1145 cm^{-1}, RbO_2: 1141 cm^{-1} [22]). CsO_2 has the largest lattice parameters, resulting in a larger distance between the dioxygen dumbbells and cesium and hence a lower cationic field felt by the dumbbells. This lowers the stretching mode frequency. A broad feature with low intensity centered at 800 cm^{-1} was also observed in the spectra. This indicates the presence of a very low concentration of peroxide anions, which might result from incomplete oxidation.

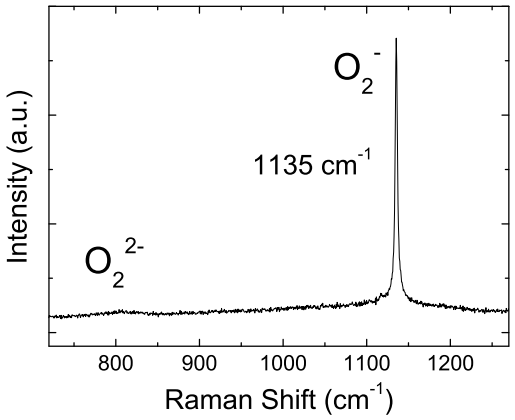

Figure 5.3. Raman spectrum of CsO_2 at room temperature. The intense peak at 1134 cm^{-1} is the O-O stretching mode of the superoxide anion.

5.4 Magnetic Properties

5.4.1 One-Dimensional Spin Chain

The dominant feature in the magnetic susceptibility of polycrystalline CsO_2 is the broad maximum centered at ∼28 K (Figure 5.4). This broad maximum is very similar to that measured by Zumsteg et al. shown in Figure 5.1(a). However, the origin of this feature was not previously discussed or studied. Considering the spin glass behavior observed in Cs_4O_6 [23] and $RbO_{1.66}$ (Chapter 4), which often gives a broad susceptibility maximum, this possibility was reinvestigated in CsO_2. However, the following typical features of spin glasses were absent. First, no significant irreversibility was observed between the field-cooled and zero field-cooled susceptibility at any temperature. Second, the magnetization showed no dependence on time (thermoremanent magnetization). The broad peak in the magnetic susceptibility versus temperature curve is thus likely to be indicative of a low-dimensional magnetic system [24, 25]. The spins in superoxide anions are known to be perpendicular to the molecular axis [18]. However, the spins are free to rotate in the plane perpendicular to the molecular axis. There are no other interactions (e.g. dipole-dipole interactions that can be relevant in Ising-type systems) that restrain the directions of the spins with respect to the dimensionality of the magnetic ordering. However, the dumbbells tilt away from the *c*-axis at low temperature such that the spins deviate from an XY geometry, as described later. Although the g-tensor for CsO_2 determined by EPR is moderately anisotropic ($g = 2.66$ parallel to [001] and $g = 1.90$ perpendicular to [100]) [18], the system follows Heisenberg-type behavior reasonably well, as shown below.

Because there is one unpaired electron in the π anti-bonding level of the O_2^- molecule, superoxide is commonly regarded as a S = 1/2 system (this is confirmed below by the effective moment obtained from a Curie-Weiss fit). The broad feature in the susceptibility curve is well fitted by the S = 1/2 square lattice Heisenberg model recently formulated by Keith et al. [12]:

$$\chi^*(\alpha,T) \equiv \frac{\chi(\alpha,T)2J}{Ng^2\mu_B^2} \equiv \frac{\chi(\alpha,T)2J}{Ck_B} = \frac{1}{4T}\frac{\sum_{n=0}^{6}[N_n\left(\frac{J}{T}\right)^n]}{\sum_{n=0}^{6}[D_n\left(\frac{J}{T}\right)^n]}, \tag{5.1}$$

where

$$N_0 = D_0 = 1, \tag{5.2}$$

$$N_n(\alpha) = \sum_{m=0}^{4} N_{nm}\alpha^m, \tag{5.3}$$

$$D_n(\alpha) = \sum_{m=0}^{4} D_{nm}\alpha^m. \tag{5.4}$$

The Hamiltonian of this system is written as:

$$\vec{\mathcal{H}} = J\sum_i \left[\vec{S}_i \cdot \vec{S}_{i+x} + \alpha\vec{S}_i \cdot \vec{S}_{i+1}\right]. \tag{5.5}$$

The parameter α in the above equations denotes the ratio between two orthogonal exchange interactions, i.e. $J' \approx \alpha J$. For 2D antiferromagnetic ordering on a square lattice, J and J' are equal and $\alpha = 1$, whereas $\alpha = 0$ signifies an antiferromagnetic spin chain. The model can also be applied to 2D systems incorporating mixed antiferromagnetic and ferromagnetic interactions, for which -1 $\leq \alpha <$ 0. However, attempted fits in which α was constrained to have a negative value resulted in α = -0.000001. This indicates that there are no ferromagnetic interactions in CsO_2. Thus, the limiting case where -1 $\leq \alpha <$ 0 is not relevant here and will not be further discussed in this chapter. Three parameters are fitted using Eq. 5.1: α, C and J/k_B.

The fit to the broad peak using Eq. 5.1 and a non-linear least-squares algorithm is shown in Figure 5.4(a). The fit yields J/k_B = 20.27 K, α = 0 and C = 0.325. The zero value of α implies that the system is essentially an antiferromagnetic spin chain. This finding is in agreement with an alternative method of fitting the susceptibility using Feyerherm's S = 1/2 Heisenberg antiferromagnetic chain model [26]:

$$\chi = \frac{Ng^2\mu_B^2}{4(2J)t}\frac{t^3 + 0.08516t^2 + 0.23351t}{t^3 + 0.73382t^2 + 0.13969t + 0.53568}, \tag{5.6}$$

where

$$t = \frac{k_BT}{2J}. \tag{5.7}$$

Feyerherm's polynomial approximation was obtained from Bonner and Fisher's formulation for linear chains of S = 1/2 spins [13]. Using this polynomial model, the exchange parameter J/k_B is determined to be 20 K. The fit using Eq. 5.6 is shown in Figure 5.4(b). Moreover, both models fit the data well up to 65 K, above which paramagnetic behavior is observed. The origin of the one-dimensional antiferromagnetic chain will be further explained in the discussion section.

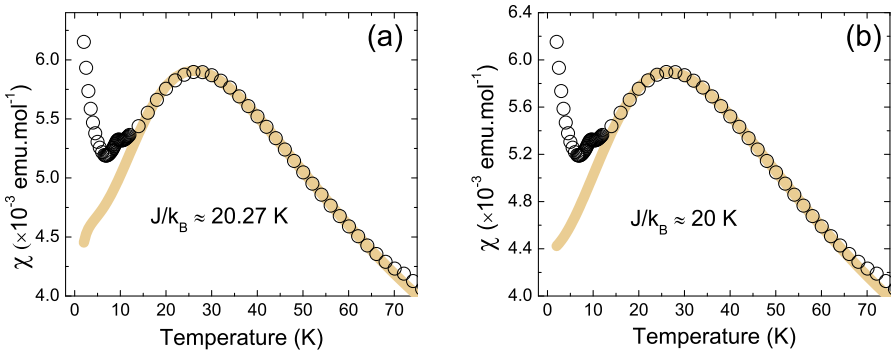

Figure 5.4. (a) The magnetic susceptibility versus temperature of polycrystalline CsO_2 fitted with Eq. 5.1; (b) fitted with Eq. 5.6. The broad peak with a maximum at 28 K indicates an antiferromagnetic Heisenberg spin-chain.

A slope change in the magnetic susceptibility is apparent at 70 K and coincides with a structural phase transition (see section 5.5). In Figure 5.5(b) this slope change is obvious when the derivative of the susceptibility is plotted. The inverse susceptibility was fitted in the paramagnetic region ($T > 150$ K) using the Curie-Weiss equation:

$$\chi(T) = \chi_o + \frac{C}{T + \theta_{cw}}. \tag{5.8}$$

The fitting includes a temperature independent term (χ_o), which contains the correction to the magnetic moment due to the diamagnetic contribution from the sample surroundings (i.e. NMR tube, plastic straw). The fitted Curie-Weiss temperature (θ_{cw}) was -40.3 K, which indicates predominant antiferromagnetic interactions. The effective moment (μ_{eff}) was 2.03 μ_B, which is greater than 1.73 μ_B expected for a S = 1/2 system and suggests the presence of a significant orbital moment.

Long-range antiferromagnetic ordering of CsO_2 was previously reported to set in below 9.6 K on the basis of magnetic susceptibility and EPR measurements, as well as a peak in the specific heat shown in Figure 5.1(a) [18, 21]. This is consistent with the small peak in the magnetic susceptibility of the sample shown in Figure 5.4(b). However, the origin of the low temperature susceptibility tail

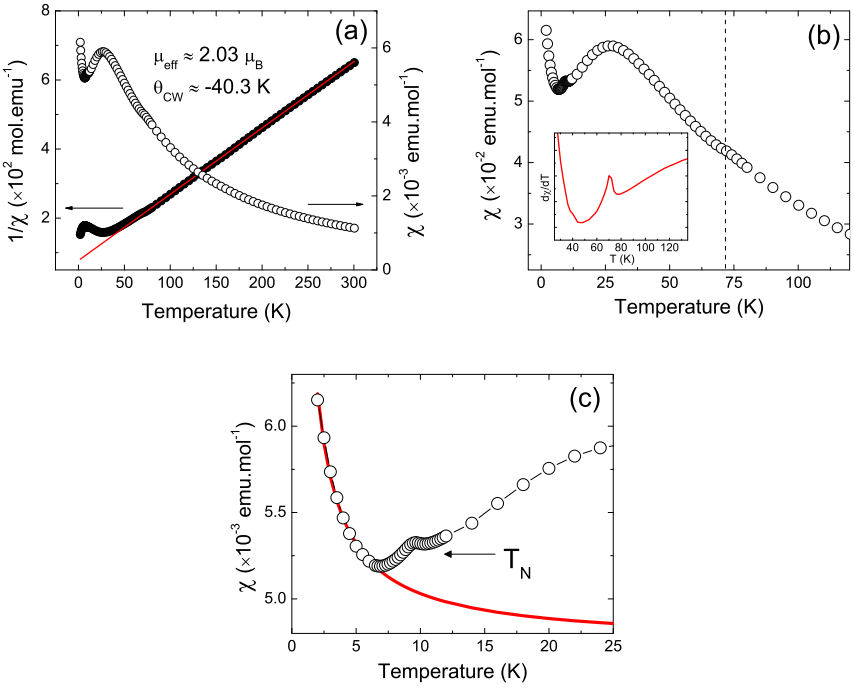

Figure 5.5. (a) Magnetic susceptibility and inverse susceptibility of polycrystalline CsO_2 as a function of temperature measured in field-cooled (FC) mode at H = 10 kOe. The red line is a fit to the Curie-Weiss law above 150 K. (b) Slope change around 70 K which can be attributed to a structural phase transition (inset: plot of dχ/dT vs T, emphasizing the slope change. (c) Fitting of the Curie tail at low temperature. The peak at 9.6 K indicates the Neel temperature (T_N) of the 3D antiferromagnetic ordering.

below 7 K (Figure 5.5(c)) is rather unclear. An diverging susceptibility at zero temperature is often related with the occurrence of unpaired spins at the ends of spin chains with odd number of spins [13]. A diverging susceptibility at T = 0 K also signals the absence of an excitation gap. Moreover, the prediction of the occurrence of unpaired spins has to be accompanied by the absence of 3D ordering below the spin-chain ordering region. Nevertheless, the experimental evidence strongly suggests that the low temperature susceptibility tail arises within a 3D antiferromagnetically ordered state. It is unclear whether the low temperature susceptibility tail is associated with the 3D antiferromagnetic ordering. A fit to the low temperature tail using the function $\chi = \chi_o + C/T$ (Figure 5.5(c)) gives C $\sim$ 0.003 emu.K/mol (effective moment of $\sim$0.15 μ_B/formula unit). Without ruling out the possibility that the tail corresponds to spins at the ends of the chains, the small number of unpaired spins might also result from local structural defects or disorder.

5.4.2 Field Dependence of Magnetization

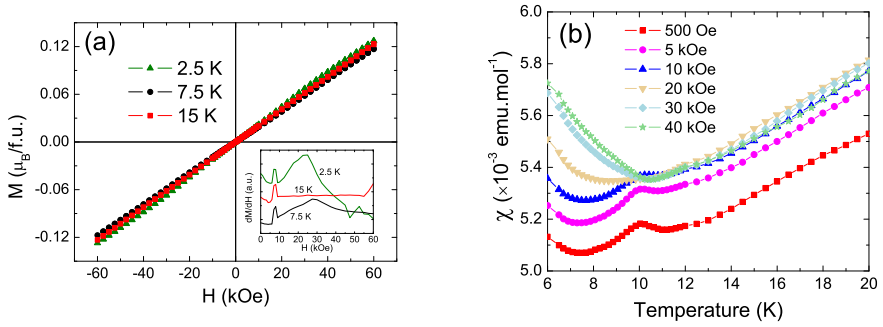

Figure 5.6. (a) Magnetization as a function of magnetic field at different temperatures (2.5, 7.5, and 15 K). The inset shows the derivatives of the curves. (b) Zero-field-cooled magnetic susceptibility as a function of temperature measured on warming in different magnetic fields.

The magnetization was measured as a function of magnetic field and is shown in Figure 5.6(a) for three different temperatures. A linear dependence of the magnetization on field was observed in each case, although the 2.5 K data curve slightly in the vicinity of 28 kOe. This effect is more clearly seen in the derivative of the magnetization (inset of Figure 5.6(a)), which shows a maximum centered at 28 kOe. Labhart et al. mentioned that a spin-flop phase transition at 28 kOe exists in CsO_2 [18]. This statement was based on experimental evidence shown by Zumsteg et al. [21], who regarded an anomaly in the adiabatic differential susceptibility at 28 kOe as a metamagnetic transition. However, a metamagnetic transition in

this system would likely involve a rotation of the dumbbells because the spins are always perpendicular to the molecular axis. The rotation of superoxide dumbbells in a magnetic field has previously been discussed for KO_2 [27–29]. This is slightly different from what one would expect for a typical metamagnetic phase transition in a highly anisotropic magnetic system, where the spin-flop transition is generally characterized by a simple reversal of the spins and results in a ferri- or a ferromagnetic state [30]. The change in slope of the magnetization at 28 kOe disappears above the Neel temperature, as seen in the inset of Figure 5.6(a). It is noted that the peaks in all the derivative curves at ∼0.9 T are an artifact involving a relaxation effect because the measurement intervals in field were different above and below this point.

The spin-flop-like transition in CsO_2 is also seen in the disappearance of the Neel temperature anomaly above 28 kOe (Figure 5.6(b), suggesting that long-range 3D antiferromagnetic ordering is suppressed at high magnetic field. The data in Figure 5.6(b) were collected on warming at a rate of 2K/min after cooling the sample from 175 K (well above the magnetic transition temperature) to 2 K in zero field. Moreover, the low temperature susceptibility tail increases with increasing magnetic field as the 3D ordering becomes shorter range. This is consistent with the statement that this tail arises from paramagnetic impurities.

5.5 Low-Temperature Crystal Structure

Figure 5.7(a) shows the X-ray diffraction pattern of CsO_2 at 20 K, which looks similar to that at room temperature except that peaks with $h \neq k$ are broadened or split. For example, the 200 peak at $2\theta = 41.75°$ splits into a $200 + 020$ doublet (Figure 5.8(b) and (c)), which indicates an orthorhombic distortion of the unit cell. The XRD patterns were indexed such that $b > a$ and good fits could be obtained using the space group $Immm$. In this symmetry the Cs atoms remain at the unit cell origin, whereas the dioxygen anions are free to tilt away from the c-axis. The refinements suggested that the tilt angles are small with respect to c, being no more than 5° at 20 K. From the quality of the fit alone one can not conclude whether the tilting is in the ac or bc plane, but the latter is assumed due to the elongated b-axis. It was necessary to apply a soft constraint to the oxygen-oxygen distance in order to keep it in the range 1.32 Å to 1.33 Å for the superoxide anion. Figure 5.7(b) illustrates the orthorhombic structure. As seen in the figure, the dumbbell tilts are disordered in opposite directions in $Immm$ symmetry. The refined structural parameters are summarized in Table 5.2. In previous studies of KO_2 [31], as well as $RbO_{1.66}$ (Chapter 4), XRD data provided evidence that the dioxygen dumbbells do not only tilt at low temperature, but also shift. However, no evidence for such a feature in CsO_2 was apparent in difference Fourier plots, and the fit did not improve when structural models involving shifted dumbells were refined. It is noted that the $CsOH.H_2O$ impurity undergoes a phase transition from hexagonal to monoclinic (pseudo-orthorhombic) at 232 K [32]. Only the

Table 5.2. Refined structural parameters of CsO_2 at 20 K ($a = 4.3857(2)$ Å; $b = 4.4101(2)$ Å; $c = 7.3367(2)$ Å)

Atoms	x	y	z	U_{iso}
Cs($2a$)	0.5	0.5	0.5	0.01285(21)
O($8l$)	0	0.0301(27)	0.4081(3)	0.00315(13)

lattice parameters of the monoclinic crystal structure have been reported, but it could be modeled reasonably well by transforming the hexagonal unit cell to its equivalent orthorhombic unit cell (with no change of the c axis) and applying a small monoclinic distortion with $\beta = 90.82°$. Not being able to determine the monoclinic space group, $P\bar{1}$ symmetry was used for the refinements.

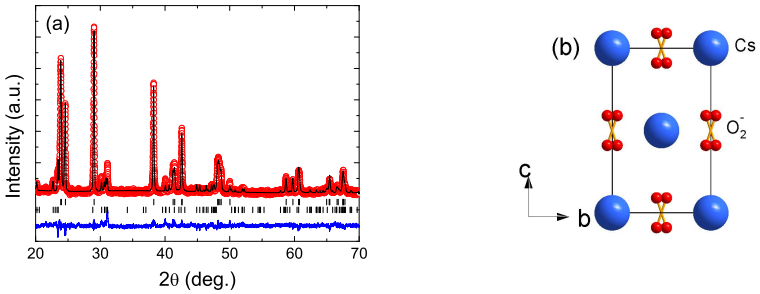

Figure 5.7. (a) Observed, calculated and difference X-ray powder diffraction patterns of CsO_2 at 20 K; upper tick marks correspond to CsO_2, lower tick marks correspond to $CsOH.H_2O$. (b) Unit cell of CsO_2 at 20 K.

Earlier work on CsO_2 single crystals reported a phase transition from tetragonal to orthorhombic at 190 K, where the superoxide dumbbells start to tilt away from the c-axis [21]. Details of the orthorhombic structure were not reported, but incommensurate satellite reflections were also observed. The current polycrystalline sample shows rather different behavior; the orthorhombic distortion sets in at ∼70 K based on the peak splitting (Figure 5.8(a)). No incommensurate peaks were observed. Moreover, there are no indications from Rietveld refinement such as unphysically large U_{iso} values or unreasonable O-O distances that could be attributed to a structural distortion at high temperatures. As seen in the figure, the splitting of the 200 peak becomes increasingly prominent below 70 K, which indicates gradually increasing tilting of the dumbbells on cooling.

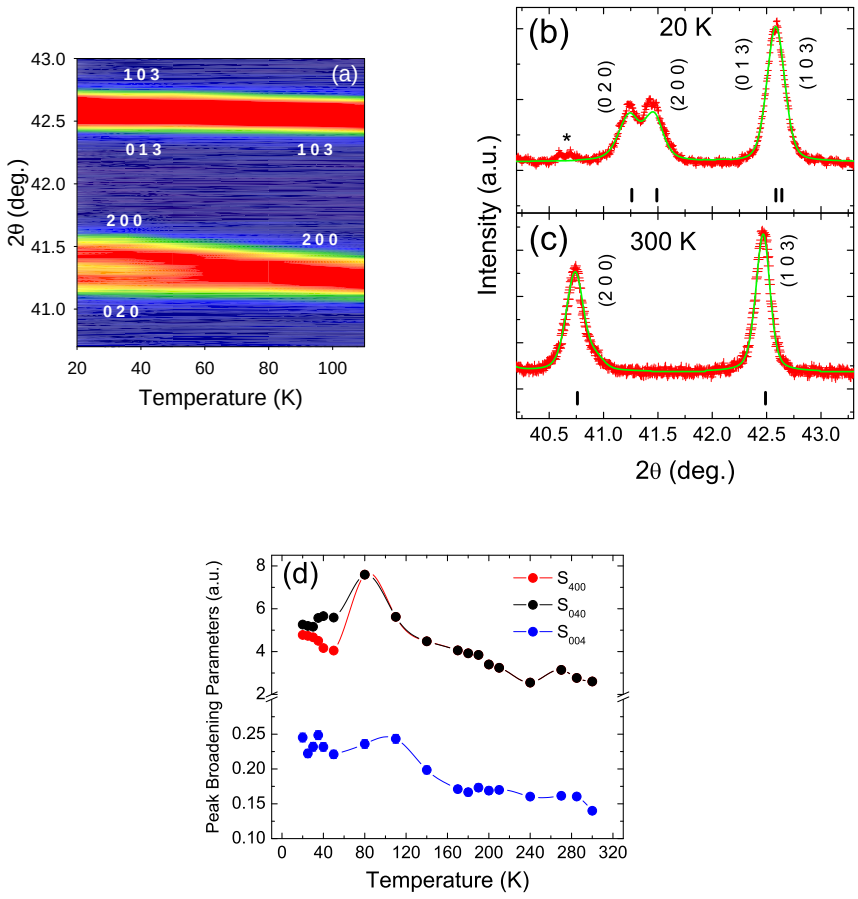

Figure 5.8. (a) Peak broadening on cooling, followed by splitting at ∼70 K, indicates a structural phase transition from tetragonal to orthorhombic. Enlarged sections of the refined x-ray powder diffraction patterns of CsO_2 are shown at (b) 20 K and (c) 300 K. (d) Microstrain peak broadening parameters as a function of temperature.

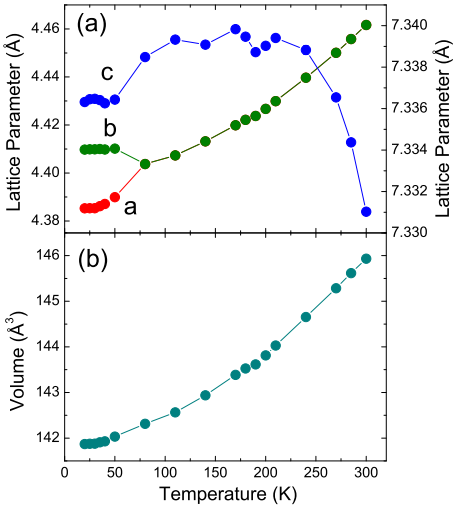

Figure 5.9. (a) The evolution of a, b, and c lattice parameters with temperature; (b) the evolution of unit cell volume with temperature.

The evolution of the lattice parameters with temperature is shown in Figure 5.9(a). Apart from the orthorhombic distortion at ∼70 K, the other noteworthy feature is a decrease of the c lattice parameter above 200 K. This can be explained as an effect of increasing thermal fluctuations on heating, where the dumbbells precess more around the c axis, allowing the axis to contract slightly. Between 200 K and 70 K the c lattice parameter can be regarded as constant, and below 70 K the c lattice parameter shortens due to coherent tilting of the dumbbells.

The refinement of anisotropic peak broadening parameters was necessary at all temperatures to fit the peak profiles properly. The S_{400} / S_{040} parameters were largest and steadily increased on cooling (Figure 5.8(d)), indicating either a degree of disorder or smaller coherently diffracting domain size in the basal plane. The S_{004} parameter is smaller at all temperatures, indicating better structural order or larger domain size in the c direction. A sudden increase of S_{400} and S_{040} coincides with the orthorhombic distortion at ∼70 K.

5.6 Low Temperature Raman Spectroscopy

Complementary to the x-ray powder diffraction results, Raman spectra were measured at different temperatures in order to get more insight into the crystallographic behavior of polycrystalline CsO_2. It has been mentioned in the previous

section that CsO_2 undergoes a phase transition at ∼70 K from a high-temperature tetragonal structure in which the dumbbells are oriented along the *c*-axis to a low-temperature orthorhombic structure in which the dumbbells are slightly tilted away from the *c*-axis. Group theoretical analysis was performed in order to analyze the molecular and lattice vibrations that can occur in both structures (tetragonal and orthorhombic).

In the high-temperature tetragonal structure ($I4/mmm$, point group D_{4h}^{17}), using group theoretical analysis one can derive all the possible optical modes [33, 34]. Cesium (Cs) in the tetragonal phase, with multiplicity = 2, has D_{4h} symmetry. Oxygen, with multiplicity = 4, has C_{4v} symmetry. The optical modes that can be expected to emerge in the high-temperature tetragonal structure are given by:

$$\Gamma^{op}(D_{4h}) = A_{2u} + E_u \tag{5.9}$$

$$\Gamma^{op}(C_{4v}) = A_{1g} + A_{2u} + E_g + E_u \tag{5.10}$$

From these equations it is clear that only 2 Raman active modes can be expected in the tetragonal structure: $A_{1g} + E_g$. One of these is the normal (stretching) mode, Σ_g^+, of the oxygen dumbbell (superoxide), which has $D_{\infty h}$ symmetry. As was discussed by Bates et al., this Σ_g^+ mode is responsible for the presence of the A_{1g} component in the predicted optical modes [22]. This stretching mode is characteristic of superoxide, and always appears in the range between 1130 cm^{-1} and 1145 cm^{-1} depending on the local environment [22, 35–37]. The E_g component in the predicted optical modes is probably a lattice (phonon) mode. It is noted that $I4/mmm$ symmetry does not allow a mode originating from Cs (Wyckoff position $2a$). All Raman active modes in $I4/mmm$ are originating from the oxygen. Figure 5.10 shows regions of the measured Raman spectrum of tetragonal CsO_2 at 110 K (well above the structural phase transition). Only two modes appear: a sharp peak at 1134 cm^{-1} and a broad peak in the vicinity of 75 cm^{-1}. The sharp peak at 1134 cm^{-1} is the superoxide stretching mode (A_{1g}), whereas the broad peak at low wavenumber can be assigned to the phonon mode with E_g symmetry.

In the low-temperature structure ($Immm$, point group D_{2h}^{25}), it is predicted that there are 6 Raman active modes (subscripted g (gerade) in Eq. 5.11), and all the modes are assumed to originate from the oxygen atoms.

$$\Gamma^{op}(D_{4h}) = 2A_g + A_u + B_{1g} + 2B_{1u} + B_{2g} + 2B_{2u} + 2B_{3g} + B_{3u} \tag{5.11}$$

Figure 5.11 shows the Raman spectrum of CsO_2 at 4.5 K (only the ranges of the spectrum where peaks appear are shown). The figure shows 4 Raman peaks at low wavenumber and a doublet at high wavenumber. The four observed Raman modes at low wavenumbers can be accounted for by theoretical calculation. Zhang et al. performed an optimization of the low-temperature CsO_2 structure using DFT (Density Functional Theory) calculations without symmetry constraints [38]. By using the unit cell parameters determined by x-ray diffraction and a supercell with doubled *b* and *c* axes (Cs_8O_{16}), the lowest energy structure had superoxide

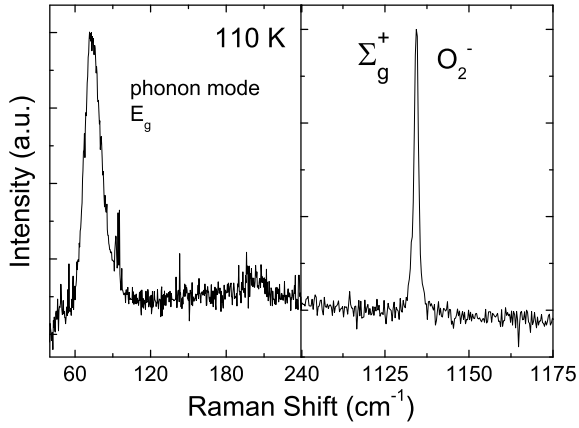

Figure 5.10. Raman spectrum of CsO_2 in the tetragonal phase (110 K).

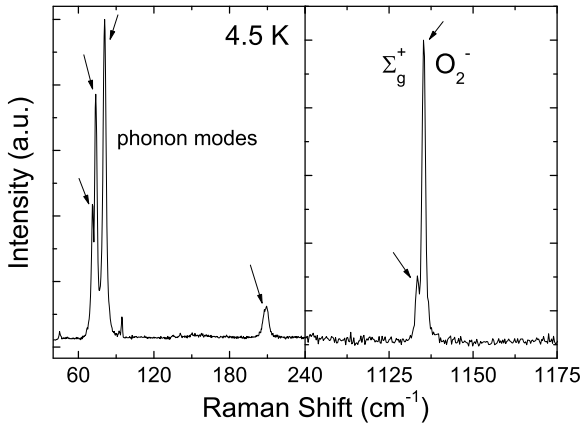

Figure 5.11. Raman spectrum of CsO_2 at 4.5 K (*Immm* space group).

dumbbells tilted by 5° from the c axis. Figure 5.12 depicts the ab plane of the optimized structure, showing 4×4 unit cells. The dumbbell tilts are essentially along the basal plane diagonal rather than the y-direction as suggested by x-ray diffraction. The tilt directions are staggered along the b-direction and uniform in the a-direction, leading to a unit cell that is doubled along b. Moreover, there are staggered shifts of the Cs cations in the a-direction, such that along the y-direction the cations form a zig-zag arrangement. This is possibly a consequence of the staggered dumbbell tilts (Cs-O electrostatic repulsive interaction). The optimized structure is similar to that calculated for KO_2 by Nandy et al. [39]. Calculations of the Raman modes using this supercell revealed four modes at low wavenumbers: 66 cm^{-1}, 67 cm^{-1}, 75 cm^{-1}, and 200 cm^{-1}. These modes agree well with the experimental spectrum in Figure 5.11. The first 3 modes from 70 cm^{-1} to 85 cm^{-1} are associated with three different interlayer motions of the Cs cations along the z-direction, and the broad feature around 210 cm^{-1} is the librational mode ("swing-like" motion) of the superoxide dumbbells. Figure 5.13 shows the temperature dependence of the three low wavenumber Raman peaks, which merge to become a single broad peak between 65 K and 110 K. Due to high thermal fluctuations, discrete and specific Cs interlayer motions no longer appear in the tetragonal structure. What is seen is a broad peak representing an average superposition of the Cs vibration/translational motions. The broad feature around 210 cm −1 (librational mode of superoxide) disappears between 65 K and 110 K. These spectral changes are consistent with the structural phase transition at ∼70 K.

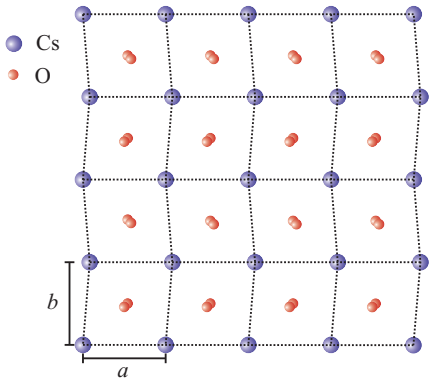

Figure 5.12. Relaxed structure of CsO_2 used for the calculation of vibrational modes and electronic density of states.

Raman active modes originating from the Cs atoms are, however, not predicted from the group theoretical analysis in the high temperature (tetragonal, $I4/mmm$) and low temperature (orthorhombic, $Immm$) symmetry. Moreover, the staggered tilt pattern of the optimized structure (Figure 5.12) is incompatible with $Immm$ symmetry; the true symmetry is likely to be lower. The O-O stretching mode (Γ_g^+)

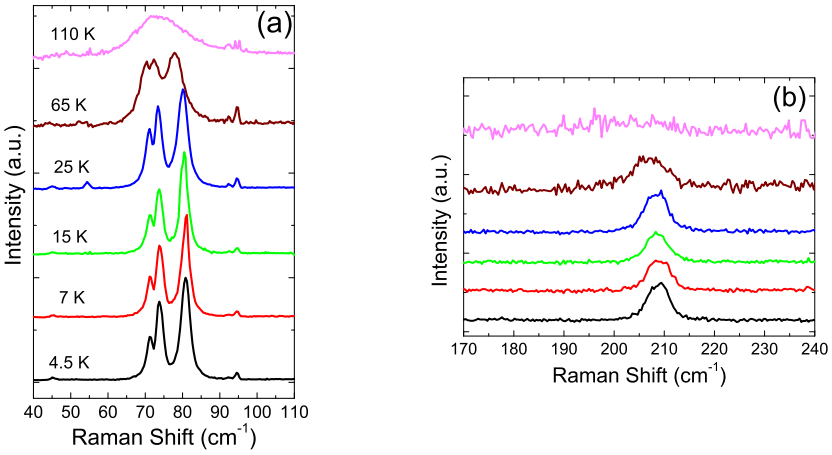

Figure 5.13. (a) Raman modes associated with the interlayer motion of Cs in CsO_2 at different temperatures. (b) The Raman peak at 209 cm^{-1} disappears in the tetragonal phase.

of the superoxide anion (1134 cm^{-1}) is present at all temperatures, except that a weaker peak appears on the low frequency side of the main peak between 110 K and 65 K (see Figure 5.14(a)).

This splitting of the superoxide stretching mode, as indicated by the presence of $2A_g$ components in Eq. 5.11, was previously reported by Bates et al. [22] and was explained in terms of a correlation field effect, similar to the case of $NaNO_3$ [40]. The expected $2A_g$ modes might not be relevant any more, since the true local symmetry is no longer $Immm$ (calculation by Zhang et al.). Devlin et al. discussed the appearance of the double A_g mode in $NaNO_3$ in terms of the presence of ordered and disordered domains. The disordered domains adopt a non-centrosymmetric structure, which leads to the appearance of a doublet. Nevertheless, the smaller peak of the doublet never dominates the main A_g mode in $NaNO_3$. A similar feature might be responsible for the doublet in polycrystalline CsO_2. The structure determined by x-ray diffraction should be considered as the average structure, which is orthorhombic with dumbbells tilted away from the c-axis. There is a chance that the local orientations of the dumbbells can vary, giving rise to domains with different chemical environments. Local variations in dumbbell orientation or environment could also be caused by site vacancies (non-stoichiometry). As is seen in Figure 5.14, there is a gradual shift of both modes to lower wavenumber with increasing temperature. Shifting to lower wavenumber can be explained in terms of lattice expansion and as a result, the crystal-field effect

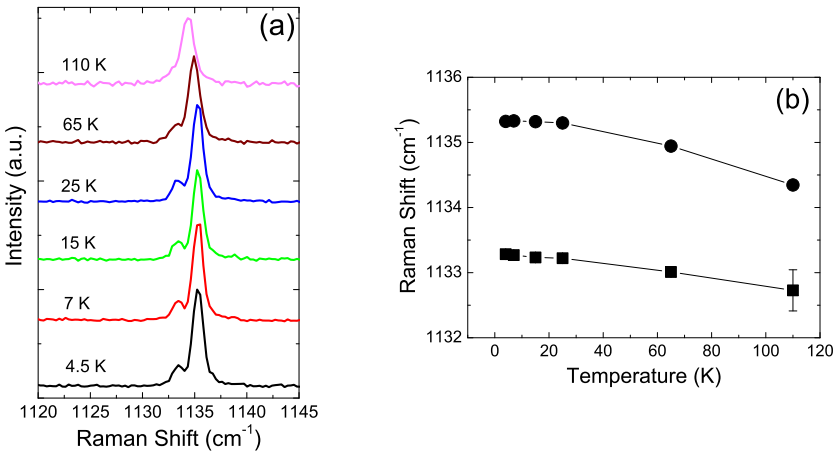

Figure 5.14. (a) Superoxide (O_2^-) stretching mode of CsO_2 shifts with temperature; (b) the peak position of the superoxide stretching mode plotted as a function of temperature.

becomes weaker due to larger atomic distances. The scenario of local defects or disorder is consistent with the low-temperature paramagnetic tail present in the magnetic susceptibility data (Figure 5.5).

5.7 Discussion

Recent studies on alkali superoxide systems suggest that there is a strong interplay between spin, orbital, and lattice degrees of freedom [39, 41–43]. Thus, one may expect a strong connection between the magnetic exchange interactions and any orbital ordering in CsO_2. At room temperature the π^* orbitals of the superoxide anion are doubly degenerate. The structural phase transition around 70 K breaks the tetragonal symmetry by tilting the dumbbells, which will lift the degeneracy of the π^* orbitals. One can draw a close analogy with the Jahn-Teller effect in transition metal oxides [44].

I will now discuss the possible magnetic exchange interactions that can occur in CsO_2 and how they can lead to the observed one-dimensional behavior. The DFT calculations performed by Zhang et al. [38] also yielded the electronic density of states, which revealed pronounced orbital ordering (OO) in the optimized structure, shown in Figure 5.15.

In this schematic picture the tilts of the dumbbells have been neglected and the molecular axes are perpendicular to the plane of the figure. The OO is similar

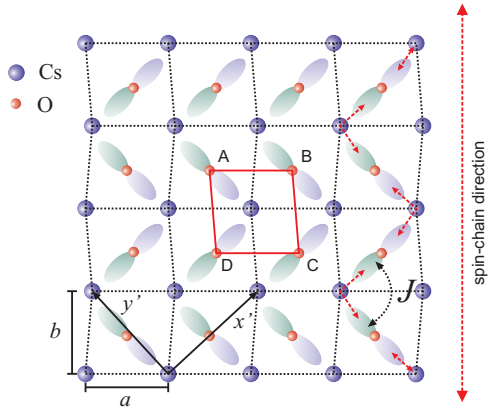

Figure 5.15. The orbital ordering of CsO_2 for the optimized low-temperature structure.

to that calculated for KO_2 by Nandy et al. [39]. The projected partial density of states showed a small difference between the spin-up and spin-down density of states. However, the total density of states for spin-up and spin-down was similar, indicating an antiferromagnetic ground state. If one look at a two-dimensional "unit cell" indicated by the red lines in Figure 5.15, there are 4 dumbbells (A, B, C, and D). Two dumbbells have half-filled orbitals with p_x character (C and D) and two with p_y character (A and B). It is important to note that x and y here refer to a new coordinate system (x' and y' in Figure 5.15), which for simplification of the calculations were chosen to be at 45° to the original coordinates [39]. There is staggered (anti-ferro) orbital ordering in the b-direction and uniform (ferro) orbital ordering in the a-direction. The lobes of dioxygen molecular orbitals never point directly towards each other, thus superexchange interactions via Cs are likely to couple the spins [8]. It is proposed that filled cesium p_z orbitals mediate the coupling along the pathways marked by red dotted arrows in Figure 5.15. Consequently, an antiferromagnetic spin chain is formed in the b-direction. The current experiments suggest that essentially no superexchange interactions occur in the perpendicular direction (a-direction). As can be seen in the figure, the uniform orbital configuration in the a-direction does not allow a superexchange pathway to form via Cs p_z orbitals or by any other form of orbital overlap. Due to electrostatic repulsion caused by the alignment of the molecular axes essentially along c, the lattice spacing in the c-direction is considerably larger and any superexchange interactions allowed by the orbital configuration in this direction (eg. $O_2\pi_x^*$ - Cs p_x - $O_2\pi_x^*$) will be much weaker due to reduced orbital overlap.

This scenario is in contrast to what has been reported for KO2 and RbO_2, which show 3D antiferromagnetic ordering at 7 K and 15 K, respectively [18]. The x-ray diffraction study of polycrystalline RbO_2 reported in chapter 3 suggested that the tilting of the superoxide dumbbells in RbO_2 is smaller than in CsO_2,

based on a smaller differentiation between the a and b axes in the orthorhombic structure at low temperatures. Magnetic susceptibility measurements on RbO_2 showed no sign of low-dimensional ordering. Because the ionic radius of Rb is smaller than that of Cs, the interatomic distances are shorter and the structure is denser. The denser structure of RbO_2 might allow magnetic exchange interactions of comparable strength along all three axes. Furthermore, the orbital ordering in RbO_2 might be different from that of CsO_2. Staggered (antiferro) orbital ordering along both basal plane axes was calculated to be most favored in RbO_2 [45], whereas in CsO_2 the orbital ordering is of ferro character along the a axis. The lattice parameter of KO_2 is even smaller. Moreover, the tilting of the dumbbells in KO_2 is much bigger. Monoclinic and triclinic structures form at low temperature. The large differences in the low temperature structures of CsO_2 and KO_2 might result in different magnetic exchange pathways.

As mentioned by Ising, an infinitely long chain cannot be achieved at finite temperatures [46]. The splitting of the 1134 cm^{-1} stretching mode of the superoxide dumbbells in the orthorhombic structure also supports the argument that the chains are of finite lengths. These chains possibly occur in domains that consist of uniformly tilted dumbbells (orthorhombic), indicated by the appearance of the most intense Raman peak. These "chain" domains might be separated by domains with disordered dumbbell tilts. As discussed above, this is consistent with the presence of a weaker peak next to the most intense stretching mode (shown in Figure 5.14(a)).

The limitation of ∼20 K in the lowest reachable temperature of the Huber G670 Diffractometer did not allow the structure to be probed below T_N. Nevertheless, one may expect that due to thermal expansion, the lattice will continue to become more compressed on further cooling. The c lattice parameter may reach a critical value at which antiferromagnetic superexchange in the c-direction becomes of significant strength. The most obvious exchange pathways are between pairs of $O_2 - \pi_x^*$ (π_y^*) orbitals via a Cs p_x (p_y) orbital. Alternatively, the 3D antiferromagnetic order might be similar to what has been observed in KO_2: ferromagnetic planes of spins are formed that are coupled in antiferromagnetic fashion [19]. In the case of a quasi-one-dimensional system, it is also possible that 3D antiferromagnetic order could arise from coupling between the chains. The 3D antiferromagnetic structure below 9.6 K in CsO_2 needs further study by neutron diffraction.

From the magnetization measurements, a schematic magnetic phase diagram of CsO_2 can be constructed (see Figure 5.16). 3D antiferromagnetic ordering, labeled AFM 1, appears below 9.6 K, above which a one-dimensional spin chain is formed due to the suppression of magnetic superexchange interactions in the other direction of the basal plane of the pseudo-tetragonal structure. A spin-flop-like phase (AFM 2) appears above 28 kOe at 2.5 K. This probably involves partial rotation of the dumbbells in the presence of magnetic field [27, 28]. The critical field for rotation decreases with increasing temperature. From the measurements of magnetic susceptibility versus temperature, the 1D antiferromagnetic spin chain persists up to at least 5 T. The temperature at which the one-dimensional ordering is des-

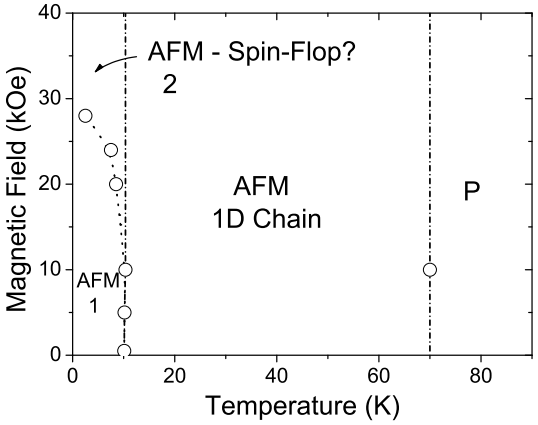

Figure 5.16. Schematic magnetic phase diagram of CsO_2.

troyed is still not clear. It is suggested that the 70 K structural transition plays a big role in destroying/creating the 1D AFM chain. Moreover, from polynomial least-squares fitting of the susceptibility data, it can be seen that the deviation of the model from the data coincides with the structural phase transition at 70 K (Figure 5.4). This suggests that the 1D AFM chain is suppressed above the transition. The complete phase diagram of CsO_2, however, needs further study.

5.8 Conclusions

Compared to the magnetic properties of the other alkali superoxides (NaO_2, RbO_2, and KO_2) and all other known inorganic p-electron magnetic systems, CsO_2 is unique in that it exhibits an antiferromagnetic spin-chain. One-dimensional antiferromagnetic ordering takes place with $J/k_B \sim 20$ K, as is confirmed by fitting the magnetic susceptibility using two independent polynomial models: (a) an S = 1/2 square magnetic lattice model [12] and (b) a 1D S = 1/2 antiferromagnetic chain model [26]. The orbital ordering (OO) state has been determined by DFT calculation. Significant orbital overlap in the b-direction mediated by the filled p_z-orbitals of cesium atoms leads to the one-dimensional chain in this direction. At 9.6 K a small peak in the magnetic susceptibility appears, indicating 3D antiferromagnetic ordering. It is suspected that inter-chain interactions become significant at this temperature. A "metamagnetic-like" phase transition under an applied field of 28 kOe involves a partial rotation of the spins, which is linked to a partial rotation of the dioxygen anions. In all of the alkali superoxides, as suggested by the current study and by earlier theoretical work, orbital ordering appears to directly drive the magnetic ordering. More experimental measurements such

as the observation of orbitons using resonant inelastic x-ray scattering [47] need to be performed in order to investigate the connection between the orbital, spin and lattice degrees of freedom in more depth. Neutron diffraction will initially be crucial in determining the magnetic structure of CsO_2. Secondly, although the onset of 3D AFM ordering is obviously seen from the specific heat curve shown by Zumsteg et al. [21], specific heat measurements over a higher temperature range need to be performed in order to confirm the 1D AFM chain nature of CsO_2.

Bibliography

[1] Bednorz, J. G. and Muller, K. A. *Z. Phys. B Con. Mat.* **64**, 189 (1986).

[2] Katsura, H., Onoda, S., Han, J. H., and Nagaosa, N. *Phys. Rev. Lett.* **101**, 187207 (2008).

[3] Furukawa, S., Sato, M., Saiga, Y., and Onoda, S. *J. Phys. Soc. Jap.* **77**, 123712 (2008).

[4] Seki, S., Kurumaji, T., Ishiwata, S., Matsui, H., Murakawa, H., Tokunaga, Y., Kaneko, Y., Hasegawa, T., and Tokura, Y. *Phys. Rev. B* **82**, 064424 (2010).

[5] Ikeda, H. and Hirakawa, K. *J. Phys. Soc. Jap.* **35**, 722 (1973).

[6] Pavarini, E., Koch, E., and Lichtenstein, A. I. *Phys. Rev. Lett.* **101**, 266405 (2008).

[7] Towler, M. D., Dovesi, R., and Saunders, V. R. *Phys. Rev. B* **52**, 10150 (1995).

[8] Kugel, K. I. and Khomskii, D. I. *Sov. Phys. Usp.* **25**, 231 (1982).

[9] Rushbrooke, G. S. and Wood, P. J. *Mol. Phys.* **1**, 257 (1958).

[10] Lines, M. E. *J. Phys. Chem. Solids* **31**, 101 (1970).

[11] Ribas, J., Monfort, M., Diaz, C., Bastos, C., Mer, C., and Solans, X. *Inorg. Chem.* **34**, 4986 (1995).

[12] Keith, B. C., Landee, C. P., Valleau, T., Turnbull, M. M., and Harrison, N. *Phys. Rev. B* **84**(10), 104442 SEP 26 (2011).

[13] Bonner, J. C. and Fisher, M. E. *Phys. Rev. A-Gen. Phys.* **135**, A640 (1964).

[14] Griffiths, R. B. *Phys. Rev. A-Gen. Phys.* **135**, A659 (1964).

[15] Fritz, J. J. and Pinch, H. L. *J. Am. Chem. Soc.* **79**, 3644 (1957).

[16] Eisenstein, J. C. *J. Chem. Phys.* **28**, 323 (1958).

[17] Haseda, T. and Kobayashi, H. *J. Phys. Soc. Jap.* **19**, 1260 (1964).

[18] Labhart, M., Raoux, D., Kanzig, W., and Bosch, M. A. *Phys. Rev. B* **20**, 53 (1979).

[19] Smith, H. G., Nicklow, R. M., Raubenheimer, L. J., and Wilkinson, M. K. *J. Appl. Phys.* **37**, 1047 (1966).

[20] Ziegler, M., Rosenfeld, M., Kanzig, W., and Fischer, P. *Helv. Phys. Acta* **49**, 57 (1976).

[21] Zumsteg, A., Ziegler, M., Kanzig, W., and Bosch, M. *Phys. Condens. Matter* **17**, 267 (1974).

[22] Bates, J. B., Boyd, G. E., and Brooker, M. H. *Chem. Phys. Lett.* **16**, 391 (1972).

[23] Winterlik, J., Fecher, G. H., Jenkins, C. A., Medvedev, S., Felser, C., Kuebler, J., Muehle, C., Doll, K., Jansen, M., Palasyuk, T., Trojan, I., Eremets, M. I., and Emmerling, F. *Phys. Rev. B* **79**, 214410 (2009).

[24] He, Z. and Ueda, Y. *Phys. Rev. B* **77**, 052402 (2008).

[25] Tsukada, I., Takeya, J., Masuda, T., and Uchinokura, K. *Phys. Rev. Lett.* **87**, 127203 (2001).

[26] Feyerherm, R., Abens, S., Gunther, D., Ishida, T., Meissner, M., Meschke, M., Nogami, T., and Steiner, M. *J. Phys.-Condens. Mat.* **12**, 8495 (2000).

[27] Bosch, M. A., Lines, M. E., and Labhart, M. *Phys. Rev. Lett.* **45**, 140 (1980).

[28] Lines, M. E. and Bosch, M. A. *Phys. Rev. B* **23**, 263 (1981).

[29] Lines, M. E. *Phys. Rev. B* **24**, 5248 (1981).

[30] Stryjewski, E. and Giordano, N. *Adv. Phys.* **26**, 487 (1977).

[31] Hesse, W., Jansen, M., and Schnick, W. *Prog. Solid State Ch.* **19**, 47 (1989).

[32] Lechner, R. E., Bleif, H. J., Dachs, H., Marx, R., Stahn, M., and Anderson, I. *Solid State Ionics* **46**, 25 (1991).

[33] Kroumova, E., Aroyo, M. I., Perez-Mato, J. M., Kirov, A., Capillas, C., Ivantchev, S., and Wondratschek, H. *Phase Transit.* **76**, 155 (2003).

[34] Rousseau, D. L., Bauman, R. P., and Porto, S. P. S. *J. Raman Spectrosc.* **10**, 253 (1981).

[35] Creighton, J. A. and Lippincott, E. R. *J. Chem. Phys.* **40**, 1779 (1964).

[36] Holzer, W., Murphy, W. F., Bernstein, H. J., and Rolfe, J. *J. Mol. Spectrosc.* **26**, 543 (1968).

[37] Blunt, F. J., Hendra, P. J., and Mackenzie, J. R. *J. Chem. Soc. Chem. Comm.* **6**, 278 (1969).

[38] Zhang, B. and de Groot, R. A. Unpublished, (2011).

[39] Nandy, A. K., Mahadevan, P., Sen, P., and Sarma, D. D. *Phys. Rev. Lett.* **105**, 056403 (2010).

[40] Devlin, J. P., Frech, R., and James, D. W. *Chem. Phys. Lett.* **12**, 602 (1972).

[41] Solovyev, I. V. *New J. Phys.* **10**, 013035 (2008).

[42] Kovacik, R. and Ederer, C. *Phys. Rev. B* **80**, 140411(R) (2009).

[43] Kim, M., Kim, B. H., Choi, H. C., and Min, B. I. *Phys. Rev. B* **81**, 100409 (2010).

[44] Novak, P. *J. Phys. Chem. Solids* **31**, 125 (1970).

[45] Ylvisaker, E. R., Singh, R. R. P., and Pickett, W. E. *Phys. Rev. B* **81**, 180405 (2010).

[46] Ising, E. *Z. f. Physik* **31**, 253 (1925).

[47] Ulrich, C., Ament, L. J. P., Ghiringhelli, G., Braicovich, L., Moretti Sala, M., Pezzotta, N., Schmitt, T., Khaliullin, G., van den Brink, J., Roth, H., Lorenz, T., and Keimer, B. *Phys. Rev. Lett.* **103**, 107205 (2009).